Long Exposure Chandra X-Ray Observation of Jupiter's Auroral Emissions During Juno Plasmasheet Encounters in September 2021

S. C. McEntee[1,2] , C. M. Jackman[1] , D. M. Weigt[3] , C. K. Louis[1] , W. R. Dunn[4,5] , A. Boudouma[6] , J. E. P. Connerney[7] , W. S. Kurth[8] , R. Kraft[9], G. Branduardi-Raymont[10] , G. R. Gladstone[11,12] , and M. J. Rutala[1]

[1]School of Cosmic Physics, DIAS Dunsink Observatory, Dublin Institute for Advanced Studies, Dublin, Ireland, [2]School of Physics, Trinity College Dublin, Dublin, Ireland, [3]Department of Computer Science, Aalto University, Aalto, Finland, [4]Department of Physics and Astronomy, University College London, London, UK, [5]Centre for Planetary Sciences at UCL/Birkbeck, London, UK, [6]LESIA, Observatoire de Paris, CNRS, PSL Research University, Meudon, France, [7]Space Research Corporation, Annapolis, MD, USA, [8]Department of Physics and Astronomy, University of Iowa, Iowa City, IA, USA, [9]Harvard-Smithsonian Center for Astrophysics, Smithsonian Astrophysical Observatory, Cambridge, MA, USA, [10]Mullard Space Science Laboratory, Department of Space and Climate Physics, University College London, Dorking, UK, [11]Space Science and Engineering Division, Southwest Research Institute, San Antonio, TX, USA, [12]Department of Physics and Astronomy, University of Texas at San Antonio, San Antonio, TX, USA

Abstract On 15 September 2021, Chandra carried out a 40-hr (~4 jovian rotations) observation as part of its longest planetary campaign to study the drivers of jovian X-ray aurora that may be linked to ultra-low frequency (ULF) wave activity. During this time, Juno's orbit had taken the spacecraft into Jupiter's dusk magnetosphere. Here is believed to be the most probable location of ULF waves propagating along jovian magnetic field lines that drive the X-ray auroral emissions. This is the first time that this region has been observed by an orbiter since Galileo >20 years ago, and never before has there been contemporaneous in situ and X-ray observations. A 1D solar wind propagation model identifies a compression event near the midpoint of the 40-hr observation window. The influence of a compression is confirmed when comparing the measured magnetic field in the dusk lobes of the magnetotail from Juno MAG data against a baseline lobe field model. Data from the Juno Waves instrument also show activation of broadband kilometric (bKOM) emissions during the arrival of the shock, a feature that has previously been observed during compression events. Therefore this is the first time we can fully analyze the morphological variability during the evolution of a shock. Wavelet transforms and Rayleigh testing are used to search for statistically significant quasi-periodic pulsations (QPPs) of the X-ray emissions in the data set, and find significant QPPs with periods of 25–26 min for the northern auroral X-rays.

1. Introduction

The first detection of X-ray emissions emanating from Jupiter was made by the Einstein Observatory (Metzger et al., 1983) in 1979, with subsequent observations made by the Röntgen satellite (ROSAT: Trümper, 1993), the Chandra X-ray observatory (CXO: Weisskopf et al., 2000), and XMM-Newton (Jansen et al., 2001). These observations have revealed distinct X-ray emissions from Jupiter's equatorial disk region and polar auroral regions. The disk emission results from elastic and fluorescent scattering of solar X-ray photons in Jupiter's upper atmosphere, meaning that this emission is largely governed by solar activity (Bhardwaj et al., 2005, 2006; Branduardi-Raymont et al., 2007, 2010; Cravens et al., 2006; Dunn, Branduardi-Raymont, et al., 2020; Elsner et al., 2005a, 2005b; McEntee et al., 2022; Wibisono et al., 2023). Jupiter's auroral emissions can be further split into two components: hard X-rays (HXRs, photons energy >2 keV) and soft X-rays (SXRs, photon energy <2 keV). The production of HXR emissions are due to bremmstrahlung radiation (Branduardi-Raymont et al., 2007), where an X-ray photon is emitted by a precipitating electron when it is deflected in the electric field of an atomic or molecular nucleus in Jupiter's atmosphere. HXRs have been found to overlap the ultraviolet (UV) main oval, leading to the conclusion that the HXR and UV auroras may be produced by the same population of energetic electrons in the middle magnetosphere (Branduardi-Raymont et al., 2008; Hill, 2001). SXRs are observed at higher latitudes than HXRs and are often located poleward of the main oval. The soft X-ray emission is thought to be a result of charge exchange processes, whereby a solar wind or iogenic ion captures a bound electron from a neutral in the jovian

atmosphere. The ion is left excited and the electron then decays to a lower energy level with the emission of an X-ray photon. This heavy ion precipitation occurs on open magnetic field lines that are connected to the solar wind or on closed field lines mapping to Jupiter's outer magnetosphere based on mapping using a flux equivalence model (Cravens et al., 1995; Dunn et al., 2016, Dunn, Gray, et al., 2020; Houston et al., 2020; Kharchenko et al., 2008; Kimura et al., 2016; Ozak et al., 2013; Vogt et al., 2011, 2015; Wibisono et al., 2021).

Jupiter's X-ray auroral emissions have been found to occasionally pulsate with statistically significant quasi-periods (Dunn et al., 2017; Gladstone et al., 2002; Jackman et al., 2018; Weigt et al., 2021; Wibisono et al., 2020). A comprehensive study of all Chandra observations of Jupiter from 1999 to 2015 revealed that, when present, the periods of the pulsations in the northern and southern auroral X-rays range from ∼8–45 min, and that these pulsations can vary on the timescale of a Jupiter rotation (∼10 hr, Jackman et al., 2018). A more recent study by Weigt et al. (2021) echoed these results when expanding the catalog to 2019 (∼2.3–36 min) to the concentrated X-ray auroral emissions. They also found these periodicities in the brightest emissions to be spatially dependent when applying a strict location criterion. Dunn et al. (2017) found that the northern and southern auroral emissions are nonconjugate in nature and can pulsate independently from each other, with different periods. Significant quasi-periodic pulsations (QPPs) are relatively rare in the jovian X-ray data (Jackman et al., 2018; Weigt et al., 2021), and the most significant pulsations almost always associate to a restrictive polar hot spot which in turn maps to a spatially localized source region in the magnetosphere (Weigt et al., 2021). The high spatial resolution of Chandra allows us to resolve the X-ray photons which comprise these hot spots, giving a unique window into the location of the driving mechanism.

Pulsations in other wavelengths have also been observed, notably including the 3–11 min period pulses in UV emission from a patch in Jupiter's polar cap (Nichols, Badman et al., 2017) and mysterious broadband radio emissions that pulsed every 10–45 min (e.g., Kurth et al., 1989; MacDowall et al., 1993). Bonfond et al. (2011) also found that the northern UV aurora exhibits flaring periodically every 2–3 min and maps to regions with closed field lines. Watanabe et al. (2018) also report periodicities of tens of minutes in the infrared (IR) aurora. Contemporaneous observations of Jupiter's auroral emissions in X-ray, UV and radio wavebands have shown that, on occasion, these multi-waveband pulsations are synchronized (Dunn, Gray, et al., 2020). The driver of this quasi-periodic emission is unknown and is one of the great open questions for jovian physics. However, in Yao et al. (2021) an interval of quasi-periodic X-ray pulsations was seen to coincide with the same pulsations in the compressional magnetic field direction and in electromagnetic ion cyclotron (EMIC) waves, which the authors used to suggest there was a causal relationship.

In this paper, we take advantage of a long (40 hr, 4 jovian rotation, JR) Chandra X-ray observation of Jupiter and compare with in situ and remote sensing data from the Juno spacecraft. At the time of the observation Juno was located in the so far unexplored dusk sector of Jupiter's magnetosphere, thought to be the most likely source region for driving of jovian X-rays (e.g., Manners et al., 2018). The arrival of a shock front at Jupiter during the Chandra 40-hr time window is detected in the tail by instruments onboard Juno. This represents the first time where it is possible to track the evolution of a shock as it propagates throughout the jovian magnetosphere with 40-hr of data. The ability to observe Jupiter's X-rays on multiple successive planetary rotations, and to combine this with in situ observation of associated fields and particles gives us the opportunity to track temporal and spatial variations in X-ray activity, the presence (or absence) of quasi-periodic pulsations, and to explore evidence for a dynamic driver of the emission.

In Section 2 we discuss the data sets used in this study and any necessary preprocessing. Section 3 outlines our analysis methods and shows results from timing analysis, including the wavelet transform to search for quasi-periodic pulsations (QPPs) and a Monte Carlo simulation to test for statistical significance. The Tao et al. (2005) solar wind propagation model, combined with in situ and remote sensing data from the radio (Waves) and magnetometer (MAG) instruments onboard the Juno spacecraft, help to provide magnetospheric context during the Chandra X-ray observation window. X-ray polar heat maps (2D histograms) are also displayed to investigate the variation in the spatial morphology over time scales of a JR (∼10 hr) and during the evolution of a possible shock propagating through the magnetosphere. A summary is provided in Section 4.

2. Data Sets and Methods

The Chandra X-ray Observatory (CXO) has several instruments on board including the High Resolution Camera (HRC-I) which can take high spatially resolved images of Jupiter's X-ray emissions. The HRC-I contains a single

large-format microchannel plate, providing spatial resolution of ∼0.4 arcsec over a 30 arcmin × 30 arcmin field of view. Time-tagged X-ray photons are recorded and then mapped to their specific location on Jupiter's surface in System III (SIII, a left-handed co-ordinate system which rotates with the planet, and where the z-axis is defined by the spin axis of Jupiter) latitude and SIII longitude using the Gaussian point spread function (PSF) of the instrument (Weigt et al., 2022). A detailed description of the methods for photon selection, pulse-invariant filtering, and correction of mapping to account for Jupiter as an oblate spheroid are described in detail in McEntee et al. (2022). The mapping algorithm assumes that the full width at half maximum (FWHM) of the HRC-I PSF is 0.8 arcsec, with an assumed PSF of 25 arcsec. The altitude at which X-ray emission occurs is assumed to be 400 km above the 1-bar atmosphere for the mapping pipeline. The scaling used for the maps is 0.13175 arcsec per pixel.

The ability to combine remotely sensed X-ray data from CXO with in situ and remote sensing data from the orbiting NASA Juno spacecraft gives us a broad insight into the temporal and spatial variability of the X-ray emissions. Additionally, we are provided with local field and plasma conditions, as well as other auroral emissions which supply context for the broad drivers of magnetospheric behavior. In this paper we complement data from the CXO (shifted backwards in time by ∼ 34 min to account for the time difference between Jupiter-Chandra and Jupiter-Juno light travel times) with data from the Juno Fluxgate Magnetometer (MAG: Connerney et al., 2017) and the Juno Waves instrument (Kurth et al., 2017). Waves is a radio sensing instrument which consists of a single electric dipole antenna mounted parallel of the spacecraft's y-axis, and a body-mounted search coil magnetometer mounted parallel to the Juno spin axis. Juno Waves measures electric field from 50 Hz to 40 MHz using two different subreceivers: the Low Frequency Receiver (LFR), from 50 Hz to 140 kHz and the High-Frequency Receiver (HFR) from 140 kHz to 40 MHz. In this study we are only using the Low Frequency Receiver. We specifically look at data from 20 to 140 kHz to isolate the broadband kilometric emissions (bKOM, Zarka et al., 2004), an auroral radio emission that is produced by the Cyclotron Maser Instability (Treumann, 2006; Zarka, 1998) at high-latitude. These emissions are influenced by changes in solar wind conditions (Zarka et al., 2021), with a sudden and intense activation during magnetospheric compression events (Louarn et al., 1998; Louis et al., 2023).

The narrowband kilometric radiation (nKOM), another component of Jupiter's radio spectrum originating from Io's plasma torus (Reiner et al., 1993), is also activated by magnetospheric compressions, although the activation is not observed until the magnetosphere is in its expansion phase (e.g., 39 hr after activation of bKOM for case study used in Louis et al., 2023). For this reason, we exclude the nKOM from the data set. We have also excluded the low-frequency (<1–20 kHz) region of the Juno Waves dynamic spectrum, containing the quasiperiodic (QP) bursts which have been found to pulse every 10–45 min (MacDowall et al., 1993). Juno's location near Jupiter's south pole during the CXO interval means that no comparisons can be made between the auroral X-ray and radio emissions and the plasma environment surrounding Juno (e.g., particle data) as no statistically significant QPPs are observed in the southern X-rays (as will be discussed later). The potential non-conjugacy of Jupiter's polar aurora (e.g., Dunn et al., 2017) also inhibits any north-south comparison.

Figure 1 shows the trajectory of the Juno spacecraft from Jupiter Orbit Insertion (JOI) until the end of 2022. The green line shows the location of Juno at the time of this observation with Juno near apojove [87.45–91.35 R_J (1 R_J = Jovian radius = 71,492 km)] from the planet on the dusk flank [20.80–20.72 Magnetic Local Time (MLT)]. The spacecraft was inside the nominal magnetopause position, and in Section 3.3. We will discuss the in situ and remote sensing Juno data which reveal the magnetospheric structure at this time.

3. Results

As mentioned in the introduction, Jupiter's auroral X-rays occasionally pulsate with statistically significant periods. The time-tagged nature of the CXO data allow us to conduct sophisticated time series analysis, while the high spatial resolution nature allow us to examine morphological features.

3.1. Temporal Analysis

Continuous wavelet transforms were applied to the entire observation to reveal if, when, and for how long the X-ray auroral emissions pulsate. The wavelet transform decomposes a function into a set of wavelets, as opposed to the Fourier transform which captures periods that persist over an entire signal/observation (Daubechies, 1990). This makes the wavelet transform better for decomposing signals which have short intervals of characteristic
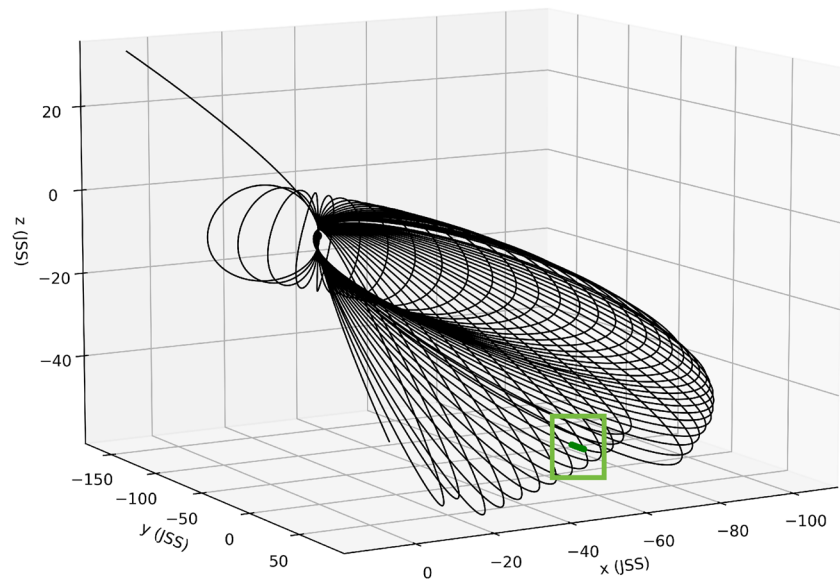
Figure 1. Juno's orbital trajectory. The location of the spacecraft during the CXO observation is highlighted in green. The green box is drawn around the relevant parts of the trajectory to highlight it. The coordinate system used here is the Jupiter-de-Spun-Sun (JSS). In this system, X points toward the Sun, Z is aligned with the jovian spin axis, and Y closes the right handed system (positive toward dusk).

oscillation, allowing it to extract both local spectral and temporal information. The time and period resolution of the power spectral density (PSD) produced by this method is low, making it difficult to determine the exact start time and period of these pulsations. However, the PSD provides a visual representation of these pulsations and gives estimates of which time intervals to investigate further using a method that does not provide simultaneous time and period resolution, such as a Rayleigh test (discussed in detail later).

Wibisono et al. (2020) found that the Shannon wavelet best replicated the known periodicities in the Jovian X-ray light curves, as it provides good period/frequency resolution, which is required for this study. Additionally, the resulting PSD clearly distinguishes each planetary rotation. Therefore we apply the same wavelet in this study. Other wavelet types, such as Gaussian and Morlet, were also tested to determine their period and time resolutions. The PSD plots for these wavelets are shown in the supporting information in Figure S1 in Supporting Information S1.

The top panel of Figure 2 shows the (light-corrected) jovian northern X-ray light curve for the entire 40 hr Chandra HRC-I observation, with the data shown in 2-min bins. The northern region includes any photons with a SIII latitude >45° (McEntee et al., 2022, see Figure 4). Emissions from the northern envelope (NE) are visible in the Central Meridian Longitude (CML) range 65–280° (e.g., Dunn et al., 2017; Jackman et al., 2018), and the gray shaded regions display when they are in view. Viewings of the NE were only considered when > half of the CML range was in view during the observation, which is why the brief interval at the beginning of the CXO observation is excluded, despite the NE being in view. Purple horizontal lines represent the length of each JR from the beginning of the X-ray observation. The bottom panel shows the PSD plot from the wavelet transform using a continuous Shannon wavelet. The color bar displays the PSD in log-form, where areas in dark red represent periods where the northern X-rays exhibit strong pulsations. As the red becomes lighter and fades to white, the significance of the pulsations decreases. Areas in blue have no regular periodicities in the light curve. The elongated finger-like structures which appear to stretch across a broad period range are a result of the binning of the data. A true quasi-periodic signal would require an intensification of PSD across a longer time-span than these finger-like structures. Figure S2 in Supporting Information S1 shows Shannon PSD plots for different time bins, which show a widening of the finger-like structures with increasing bin size.

To determine the intervals where the quasi-periodic pulsation is strongest, we set a threshold on our PSD such that log(PSD) > 2.5. This threshold was chosen in an attempt to pick out intervals of shorter duration than the NE viewings and which display strong pulsations. The time interval begins at the first time bin where the threshold
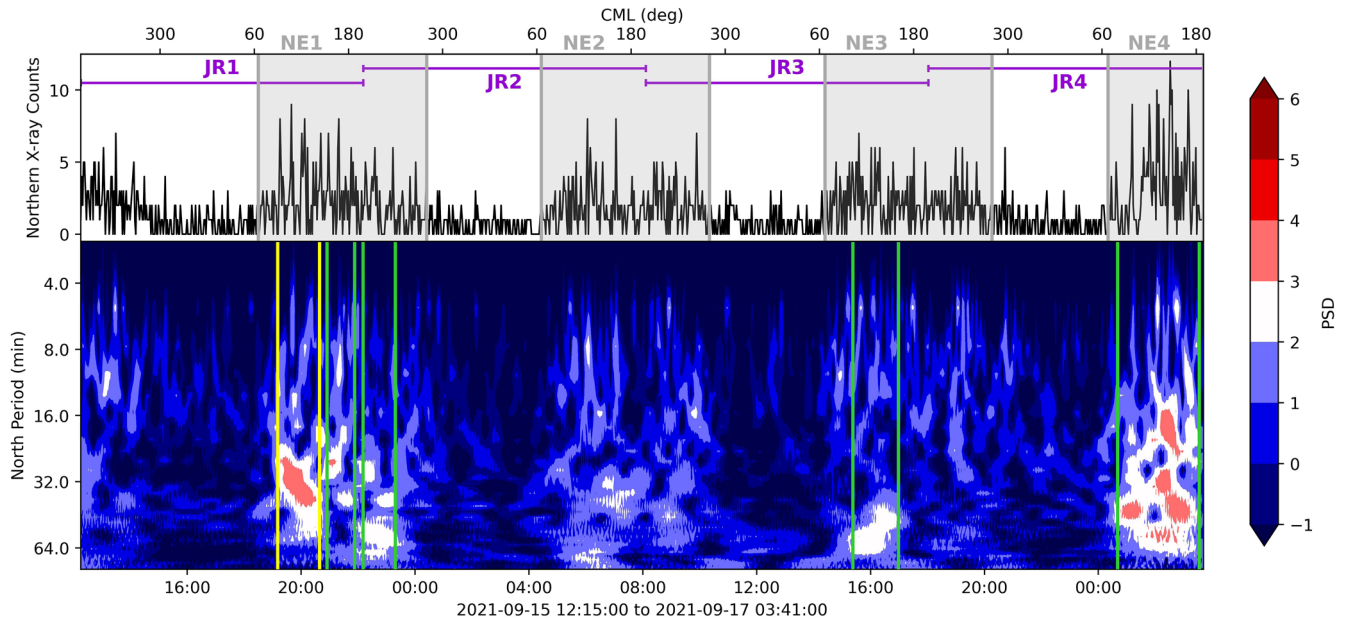
Figure 2. (Top panel) Chandra HRC-I 2-min binned jovian northern X-ray light curve. The data have been shifted backwards in time by ∼34 min to account for the time difference between Jupiter-Chandra and Jupiter-Juno light travel times during the observation. Gray shaded regions highlight when the northern envelope (NE) emissions are in view; which occur in System III CML range 65–280°. Purple horizontal lines indicate the length of each jovian rotation (JR) during the observation. (Bottom panel) Power spectral density (PSD) plot produced from the continuous wavelet transform of the 2-min binned X-ray light curve using the Shannon wavelet (2-min time resolution). The color bar shows PSD on a log scale from 2^{-1} to 2^6. Green and yellow vertical lines bracket time intervals where log(PSD) > 2.5. The time window bordered by yellow vertical lines will be presented as a case study later in the analysis.

is exceeded, and ends when log(PSD) < 2.5 for five consecutive bins (10 min). We also exclude instances where this PSD threshold was satisfied for time intervals of 30 min or less. Only considering longer-duration cases (>30 min) ensures that there were sufficient X-ray counts during the interval to perform timing analysis, and also allows a long enough duration to observe several cycles of the shorter-period pulsations previously reported in the jovian auroral literature (e.g., Bonfond et al., 2011, 2–3 min flaring in UV). Furthermore, time intervals were also selected using an analogous method, except in this instance the threshold on PSD was set such that log(PSD) > 3. The vertical green lines in the bottom panel of Figure S3 in Supporting Information S1 show the time intervals when the log(PSD) > 3 threshold was satisfied.

Table 1 presents the results of the application of the wavelet transform across the full CXO observation interval, including the start times, end times, and durations of any time intervals of interest. Within this 40 hr CXO observation of Jupiter, containing four viewings of the northern envelope (NE), we identify five time intervals where our log(PSD) > 2.5 condition was satisfied (indicated in bottom panel of Figure 2). Three of these time intervals happened during the first viewing of the northern envelope (NE1: 2021-09-15 18:29 to 2021-09-16 00:24). The first began at 19:10 UT on 15 September 2021 during the first viewing of the northern envelope (NE1), and lasted for 88 min, showing a range of pulsation periods of ∼20–40 min. During this window, 124 X-ray counts were detected by Chandra HRC-I. This interval is bracketed by yellow vertical lines in Figure 2 and will be analyzed further in the next section. We also observe a much longer time interval where this PSD threshold was exceeded near the end of the observation, beginning at 00:40 UT on 17 September 2021 during NE4, and lasting for a duration of 172 min. In this example, we observe 290 counts, and see an intensification in PSD over a broader range of periods, from ∼10–50 min. The most intense regions take the shape of small patches joined together, as opposed to one extended structure as is seen in the first example.

The wavelet transform of the entire ∼40 hr jovian northern X-ray light curve identified pulsating intervals that required further analysis using Rayleigh testing (Leahy et al., 1983; Mardia, 1972) to identify any (quasi-)periodic behavior. The Rayleigh technique can be applied to unbinned, irregularly sampled data and thus is well suited to the time-tagged photon data detected by CXO. The Rayleigh test is particularly suitable for a sparse count regime, and this is why we use it to analyze Jupiter's low X-ray photon count as detected by Chandra HRC-I instead of other methods such as fast Fourier transforms and Lomb-Scargle analysis. In this method, each time-tagged photon is

Table 1
Rayleigh Test Results for Time Intervals Identified Using Constraints on Central Meridian Longitude (CML) and Latitude (Lat), Power Spectral Density (PSD) Threshold of log(PSD) > 3, and log(PSD) > 2.5.

	Constraint	Start time (Y-M-D hr:min)	End time (Y-M-D hr:min)	Duration (min)	Total Counts	Best period (min)	Max power (arb. units)	p-value
NE1	**CML + Lat**	**2021-09-15 18:29**	**2021-09-16 0:24**	**355**	**389**	**25.745**	**16.252**	**0.0003**
	PSD > 3	2021-09-15 19:18	2021-09-15 20:32	74	101	23.941	13.075	0.0271
	PSD > 2.5	**2021-09-15 19:10**	**2021-09-15 20:38**	**88**	**124**	**25.114**	**21.974**	**0.0004**
		2021-09-15 20:54	2021-09-15 21:52	58	79	24.32	7.891	0.8891
		2021-09-15 22:10	2021-09-15 23:18	68	71	48.472	11.026	0.0331
NE2	CML + Lat	2021-09-16 04:26	2021-09-16 10:20	355	341	28.621	6.143	0.6804
	PSD > 3	–	–	–	–	–	–	–
	PSD > 2.5	–	–	–	–	–	–	–
NE3	CML + Lat	2021-09-16 14:24	2021-09-16 20:15	352	369	4.839	8.139	0.1917
	PSD > 3	–	–	–	–	–	–	–
	PSD > 2.5	2021-09-16 15:22	2021-09-16 16:58	96	118	39.702	14.14	0.0301
NE4	CML + Lat	2021-09-17 00:20	2021-09-17 03:41	201	319	29.443	9.683	0.2024
	PSD > 3	2021-09-17 00:48	2021-09-17 03:22	154	276	41.872	12.192	0.0435
	PSD > 2.5	2021-09-17 00:40	2021-09-17 03:32	172	290	28.097	10.15	0.1413

Note. The start time, end time, and duration (in minutes) are shown for each interval. Results include total counts, period corresponding to max power (minutes), max Rayleigh power (in arbitrary units), and *p*-value of statistical significance. Test was carried out for 10,0000 Monte Carlo simulations. Cases where a quasi-periodic pulsation was found with statistical significance >99% (*p*-value < 0.01) are shown in bold.

associated with a phase for each assumed frequency and we examine whether the distribution of phases is uniform, or whether there are any local anomalies. A uniform distribution indicates that no period is detected in the time series (i.e., the null hypothesis), while an anomalous distribution suggests there may be a significant quasi-period present (i.e., rejecting the null hypothesis). A power spectrum is then generated where the highest power results from smooth, quasi-sinusoidal, periodic signals, while sharp pulses can cause high powers at the harmonics associated with their fundamental frequency (Jackman et al., 2018). Monte Carlo simulations consisting of randomly shuffled light curves that contain the same number of photons over the same time interval as the real input data, but with randomised photon arrival times, are used to evaluate the statistical significance of any quasi-periods found in the X-ray data. The same Rayleigh analysis is then performed for 10,000 *fake* light curves using an identical frequency grid. This allows us to estimate the likelihood that a light curve without a periodic signal present could produce a peak power greater than that observed in the jovian X-ray light curve (null hypothesis).

A Rayleigh test was performed on the highlighted time intervals in Figure 2. This included the full viewings of the jovian northern auroral region (SIII CML range 65–280°, SIII lat > 45°) highlighted in gray in the top panel of Figure 2, along with the shorter time intervals identified from the wavelet transform (green and yellow vertical lines in bottom panel of Figure 2). Additionally, time intervals were also selected using the alternative log(PSD) > 3 threshold (see Figure S3 in Supporting Information S1 for time intervals). The results of the Rayleigh test are displayed in Table 1, displaying the total counts of the input data, the quasi-period corresponding to the peak power, the peak power (in arbitrary units) found in the input light curve, and the statistical significance of the quasi-periodic pulsation.

3.2. Pulsating Northern Hot Spot

Of the different time intervals selected for Rayleigh testing in Table 1, only two contain a quasi-period that is >99% statistically significant (*p*-value <0.01): the first full viewing of the northern envelope using the SIII CML plus latitude constraint (NE1: first gray shaded region in top panel of Figure 2), and the first time interval during the first northern envelope viewing where the log(PSD) > 2.5 threshold was satisfied within the wavelet transform (vertical yellow lines in bottom panel in Figure 2). Figure 3 shows the Rayleigh test results for the latter of these two time intervals, beginning at 19:10 UT and lasting for a duration of 88 min. In this time window, 124 photons were detected, and Figure 3a displays a 60-s binned light curve of the input data. It should be noted that the binned light curve is not used in the analysis and is presented solely for visual purposes. Figure 3b shows the
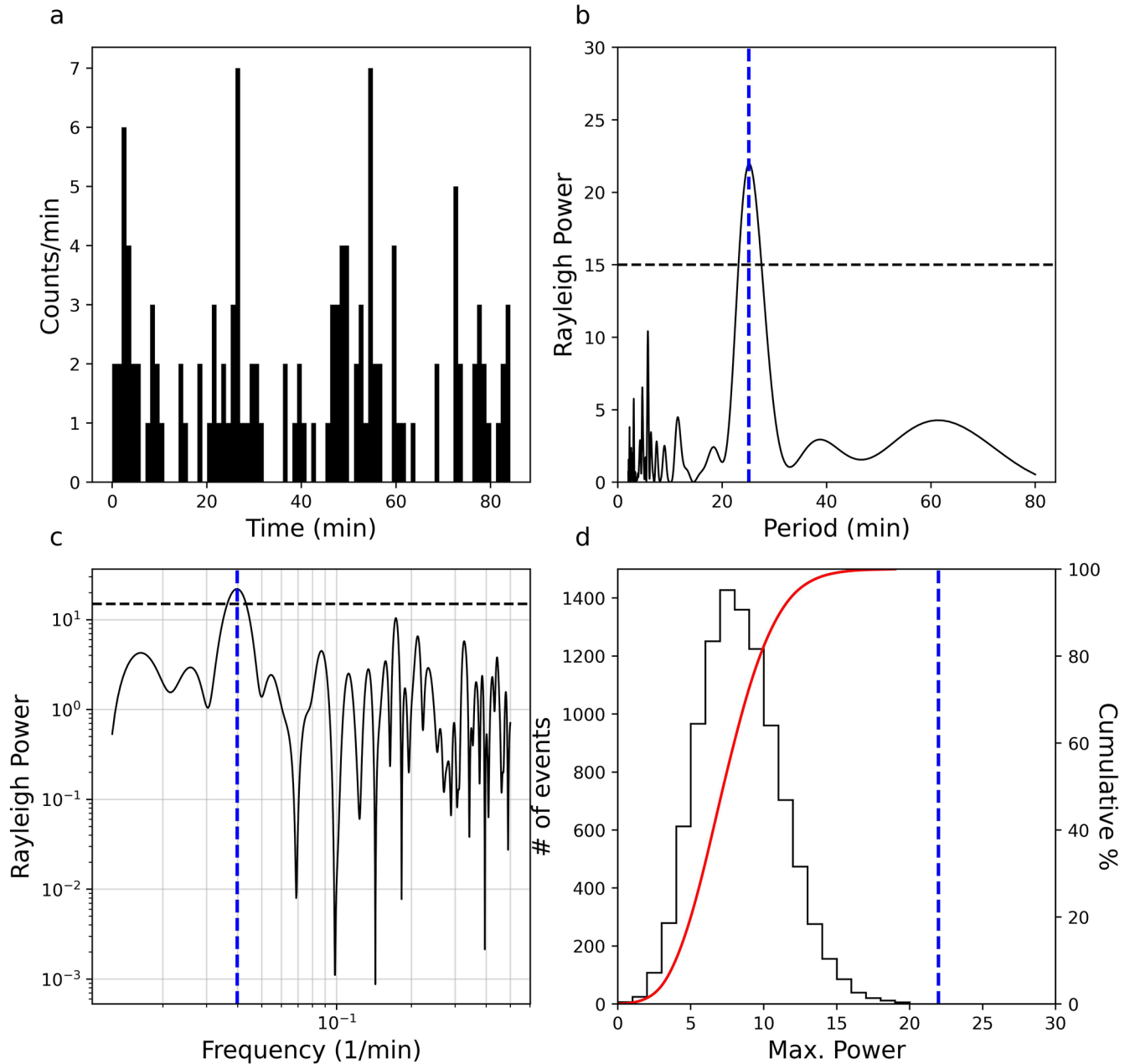
Figure 3. Results from the Rayleigh test performed on identified pulsating interval from wavelet transform. (a) Jovian 60-s binned northern X-ray light curve of time-tagged photons from 19:10 to 20:38 UT. (b) Rayleigh power (in arbitrary units) versus period from the Rayleigh test on input light curve. The quasi-period corresponding to the peak power (~25.1 min) is indicated by a vertical blue dashed line. The horizontal dashed line represents the 99th percentile of the power from the 10,000 Monte Carlo simulations. (c) Power versus frequency from the Rayleigh test in log-log scale to investigate power law behavior associated with red noise. (d) Histogram of maximum powers from the Rayleigh analysis of 10,000 randomly generated light curves based on the original data. The peak power (associated with best quasi-period from the original data) is denoted by the vertical blue dashed line. The red line shows the cumulative probability distribution of the maximum powers.

Rayleigh power (in arbitrary units) as a function of period. The period corresponding to the peak power (blue dashed line) indicates the best quasi-period within the input light curve data, with the height of the peak related to the statistical significance of this quasi-period. In this example, the peak power is ~22 (in arbitrary units), and has a corresponding ~25.1 min quasi-period. The black dashed line shows the 99th percentile of peak power from the 10,000 randomly generated light curves. The resulting p-value of 0.0004 from the input light curve means that
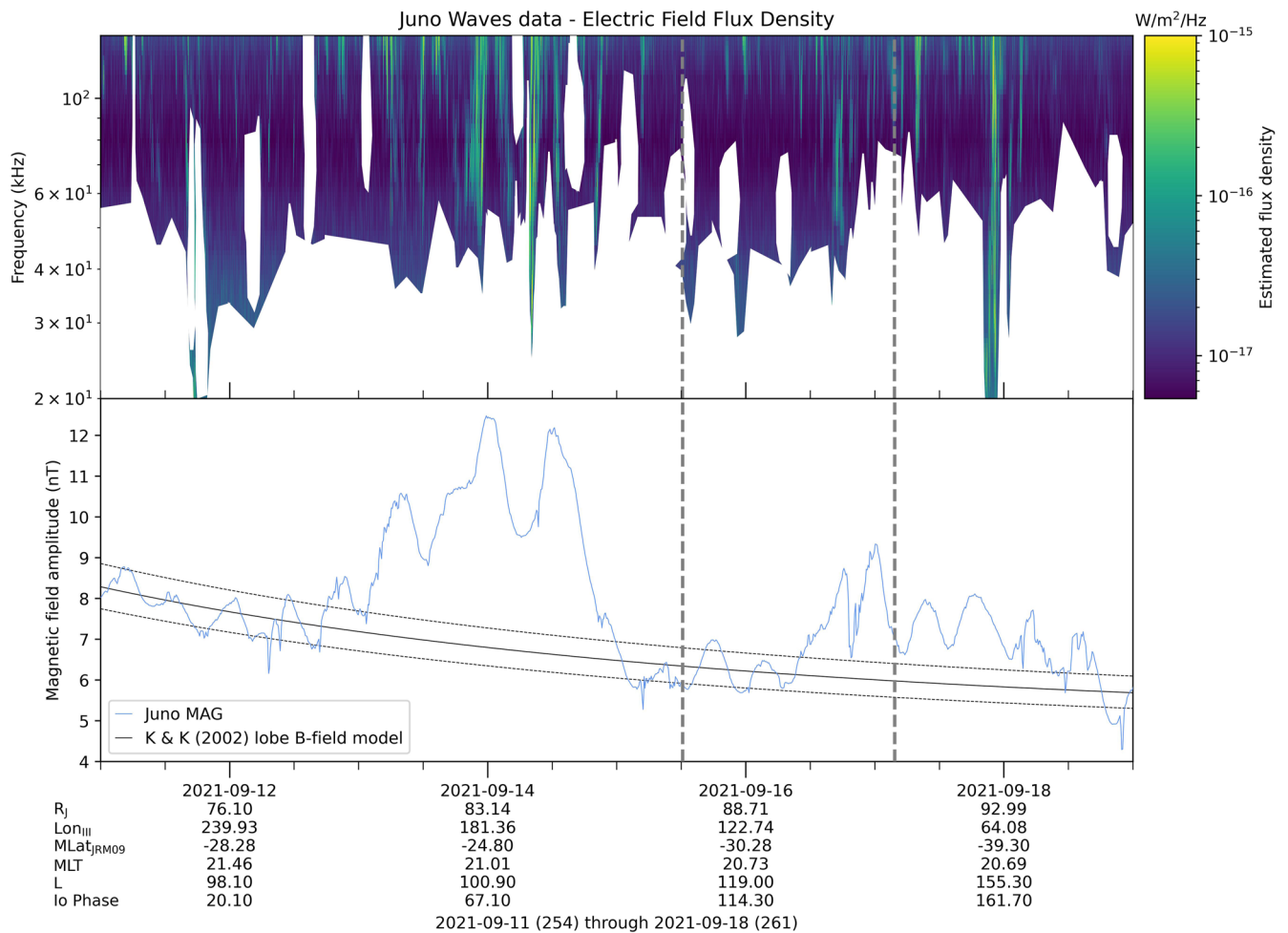
Figure 4. (Top panel) Juno Waves dynamic spectrum for 8-day interval beginning on 11 September 2021 and including ~40 hr CXO observation (dashed gray lines). Frequency is shown in log scale in the range 20–140 kHz to highlight the broadband kilometric emissions (bKOM), with all other radio emissions masked. The color bar denotes estimated flux density. (Bottom Panel) Juno MAG data (blue) with Kivelson and Khurana (2002) lobe magnetic field model (black) overlaid. Error regions are displayed as dashed black lines. Juno ephemeris data is included below *x*-axis.

only 4 of the 10,0000 *fake* light curves produced a peak power greater than the input data. Figure 3c displays the Rayleigh results in log(Power) against log(Frequency) scale. We note that the reasonably flat distribution does not provide significant evidence for a power law relation with non-zero slope, and therefore assume that there is no red noise in our data set. A histogram of the maximum powers for each of the simulated light curves is presented in Figure 3d, with the cumulative probability distribution of maximum powers overlaid in red. The blue dashed line again represents the maximum power of the input light curve data. The position of the maximum of the original data relative to the cumulative distribution shows that the highest power measured from the real data is significantly greater than what would typically be expected to emerge from analysis of randomly distributed photons lacking any periodic signal. Figures S4–S13 in Supporting Information S1 present the outputs of the Rayleigh test in the same manner as shown in Figure 3, for each of the remaining time intervals listed in Table 1. Analysis was also conducted on the southern envelope (SE) emissions, which are visible in the CML range 270-165° (Jackman et al., 2018), and have SIII lat $< -55°$ (McEntee et al., 2022). No statistically significant QPPs were found in any of the SE viewings. Additionally, at no point was either of the PSD thresholds satisfied for the southern emissions.

3.3. Accompanying In Situ Juno Data

In order to give context for the remotely sensed X-rays from Chandra, we also examine the in situ and remote sensing data taken by Juno. Figure 4 displays data from the Juno Waves (top panel; frequency range 20–140 kHz) and MAG (bottom panel) instruments over a 8-day time window beginning on 11 September 2021 and including

the 40 hr Chandra X-ray observation interval (dashed gray lines). Over this time interval, Juno's radial distance from the planet ranged from ~72–95 R_J, and the spacecraft's position in magnetic local time (MLT) was in the range 20.65–21.73 hr, located on the dusk flank of the jovian magnetosphere (see Figure 1). This dusk location was specifically chosen when planning the Chandra observation campaign as it has previously been suggested as the most likely location for the driver of the jovian auroral X-ray emission (Weigt et al., 2020, 2021; Zhang et al., 2018). One theory for the driver of these emissions is Ultra Low Frequency (ULF) waves traveling along jovian magnetic field lines which can be initiated by processes on the dusk flank of the magnetosphere (Manners et al., 2018). Alternatively, Yao et al. (2021) found that planetary-scale electromagnetic waves are observed to modulate electromagnetic ion cyclotron waves, periodically causing heavy ions to precipitate and produce Jupiter's X-ray pulses.

In the top panel of Figure 4, Juno Waves (Kurth et al., 2017) estimated flux density (Louis, Zarka, & Cecconi, 2021) are presented in the frequency range 20–140 kHz, and the color bar has been saturated to reveal the bKOM emissions. The (Louis, Zarka, Dabidin, et al., 2021) catalog of jovian radio emissions was used to identify, and then mask, any other radio emissions present in the frequency range. The bKOM is an auroral radio emissions, produced by the Cyclotron Maser Instability (Treumann, 2006; Zarka, 1998) at high-latitude. These ubiquitous drifting features are found below 150 kHz and are strongly controlled by changes in solar wind conditions (Zarka et al., 2021), with a sudden and intense activation and low frequency extension during magnetospheric compressions (Louarn et al., 1998; Louis et al., 2023).

The bottom panel of Figure 4 shows the magnetic field amplitude (blue) recorded by Juno MAG. Overlaid is the Kivelson and Khurana (2002) average lobe magnetic field model, which falls off with radial distance, ρ (in R_J), as B_{lobe} (nT) $= 2,900 \, \rho^{-1.37 \pm 0.01}$. The measured magnetic field amplitude prior to the CXO observation window is enhanced significantly above the lobe field fall off model, reaching a peak of 12.48 nT at 23:45 UT on 13 September 2021. Such behavior can be indicative of the effect of a large solar wind compression enhancing the conditions in the lobe (Jackman et al., 2010), where lobe flux content and tail flaring can be a direct response to solar wind driving. During this regime (when $B > B_{\text{lobe}}$ we also see the activation of the bKOM emissions in the Juno Waves data. These are clear signs of the activation of the bKOM due to a compression event. By the beginning of the Chandra observation at 12:14 UT on 15 September 2021, the magnetic field amplitude has fallen back down to lie within the errors of the Kivelson and Khurana (2002) lobe field model, indicating the end of this period of magnetotail inflation. The intensity of the bKOM emissions decreases over this time range, and the low frequency extension is no longer present. Another sharp spike is recorded in the MAG data toward the end of the 40 hr CXO interval, this time peaking at 9.33 nT at 00:05 UT on 17 September 2021. This data gives the possibility of a second, less severe compression event, this time during the Chandra HRC X-ray observation of Jupiter. The intensity of the bKOM emissions is also observed to increase from ~15:00 UT on 16 September 2021, again with a low frequency extension during this second interval where $B > B_{\text{lobe}}$. By the beginning of the Chandra observation at 12:14 UT on 15 September 2021, the magnetic field amplitude has fallen back down to lie within the errors of the Kivelson and Khurana (2002) lobe field model, indicating the end of this period of magnetotail inflation. The intensity of the bKOM emissions decreases over this time range, and the low frequency extension is no longer present. Another sharp spike is recorded in the MAG data toward the end of the 40 hr CXO interval, this time peaking at 9.33 nT at 00:05 UT on 17 September 2021. This data gives the possibility of a second, less severe compression event, this time during the Chandra HRC X-ray observation of Jupiter. The intensity of the bKOM emissions is also observed to increase from ~15:00 UT on 16 September 2021, again with a low frequency extension during this second interval where $B > B_{\text{lobe}}$.

In Yao et al. (2019), during a 5-day Juno MAG time series with similar behavior to that shown in Figure 4, it was stated that increases and decreases of magnetic field amplitude suggested that the magnetosphere was experiencing loading and unloading of magnetic energy. They also found that Hubble Space Telescope (HST) observations displayed enhanced auroral emissions at the beginning of the unloading processes, while observations during the loading processes resulted in relatively faint auroral emissions. Using this naming criterion, we infer that the jovian magnetosphere experiences two intervals of magnetic loading (increase in lobe field strength) and two intervals of magnetic unloading (decrease in lobe field strength). The magnetic loading intervals also coincide with enhancements in the bKOM emission, which is consistent with Yao et al. (2019).

3.4. Upstream Solar Wind Conditions

To get a better understanding of the state of the jovian magnetosphere in the days leading up to and during the 40 hr CXO observation time window, we compare in situ Juno Waves and MAG data with outputs from
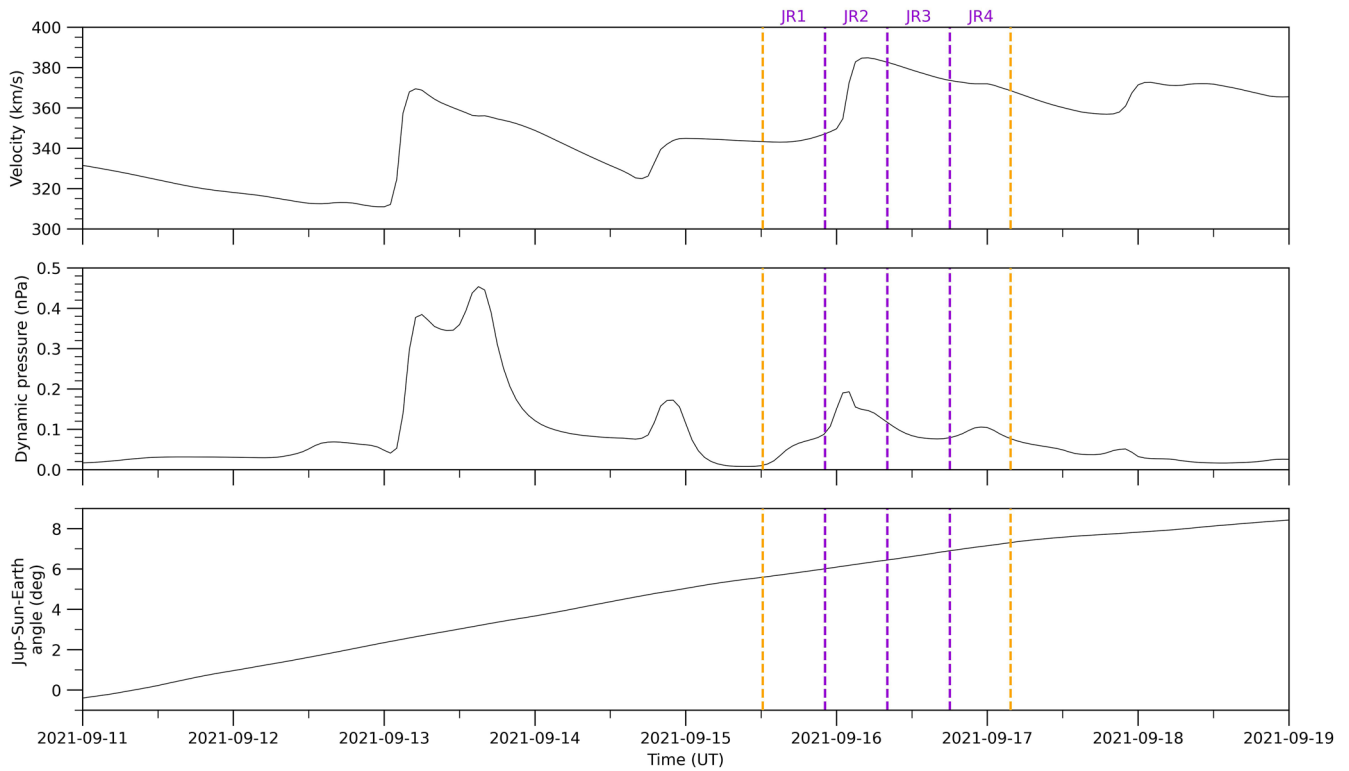
Figure 5. Results from the Tao et al. (2005) solar wind propagation model showing (a) the solar wind velocity (km/s) at Jupiter's magnetopause, (b) the dynamic pressure (nPa), and (c) the angle between Earth and Jupiter with respect to the Sun in the days leading up to and after the observation. Orange dashed lines represent time window of the light-corrected Chandra HRC-I observation. Purple dashed lines split the X-ray observation window into jovian rotations (JR).

the Tao et al. (2005) magnetohydrodynamic (MHD) solar wind propagation model. This model simulates a one-dimensional (1D) propagation of the solar wind from the Earth using OMNI data and outputs solar wind conditions at Jupiter such as solar wind velocity (v_{sw}) and dynamic pressure (P_{dyn}). The Jupiter-Sun-Earth (JSE) angle is also provided, and the Tao et al. (2005) model is best applied for cases when this angle is small (<50°) and thus the uncertainty in shock arrival time is at its smallest. Over the 8-day interval beginning on 11 September 2021, the JSE angle ranges from −2.52° to 8.43°. Tao et al. (2005) concludes that the uncertainty in the arrival time of a pressure enhancement at Jupiter is at most 2 days when the Earth-Sun-Ulysses (ESU) angles is <50°, and that the uncertainty is effectively negligible for ESU angles < 10°. As the JSE angle remains below than 10° for the entire 8 days interval, we therefore assume that the uncertainties in the propagation time from Earth to Jupiter within the Tao et al. (2005) model are minimized.

Figure 5 shows the outputs of the Tao et al. (2005) 1D MHD solar wind propagation model, displaying (a) solar wind velocity, (b) dynamic pressure, and (c) JSE angle. Orange dashed lines represent the duration of the light-corrected CXO observation interval, with purple dashed lines indicating the beginning of a new JR. The model predicts a large pressure pulse, with a peak P_{dyn} of 0.45 nPa, impacting on Jupiter's magnetosphere at 15:00 UT on 13 September 2021. This shock is accompanied by a large increase in v_{sw}, which is another indication that Jupiter's magnetosphere was in a compressed state in the days leading up to the CXO observation. Another pressure pulse is observed at 02:00 UT on 16 September 2021, with peak P_{dyn} = 0.19 nPa, again accompanied by a sharp increase in v_{sw}. This gives further credence to the idea that a compression event occurs during the 40 hr Chandra X-ray observation, as alluded to in the in situ and remote sensing Juno Waves and MAG data displayed in Figure 4.

3.5. Spatial Morphology

The high spatial resolution of Chandra HRC-I allows for detected photons emanating from Jupiter to be mapped to the planet's surface in SIII coordinates. Given the positions of the jovian photons, polar heat maps can be

generated to examine the morphology of the auroral X-rays in great detail. Figure 6 shows the polar X-ray heat maps of Jupiter's (left) north and (right) south poles, as viewed from above the pole. The plots are split into four individual JR (~10 hr) intervals to show the variation in the morphology of the auroral X-ray emission from one rotation to the next. Therefore, each panel gives the average morphology over an ~10 hr time window. The start and end times of each JR are displayed in purple, and correspond to the purple horizontal lines that were previously shown in the top panel of Figure 2. Also included are the modeled satellite footprints for Io (dashed black line) and Ganymede (solid black line), respectively. These footprints are derived from the JRM33 model (Juno Reference Model through perijove 33 Connerney et al., 2022) with the Connerney et al. (2020) magnetodisc model. The photon flux of the X-ray emission is represented by the brightness in Rayleighs (R), which is calculated from the point spread function (PSF). In total, 7,151 detected jovian photons remain after Chandra X-ray data has been processed and filtered (see McEntee et al. (2022) for full explanation of X-ray processing pipeline). Within this total photon count, 1,935 events come from the north (SIII lat > 45°), with 1,074 detections coming from the south (SIII lat < −55°) (McEntee et al., 2022). The origins of all remaining photons can be traced to the low-to mid-latitude planetary disk region, which are not the focus of this study.

Weigt et al. (2021) (from now on referred to as W21) present polar plots of the averaged X-ray emission from 28 Chandra HRC-I observations of Jupiter spanning from 2000 to 2019 (see Figure 1 in W21). They find the most intense northern emission to be located in a concentrated tear-drop shape with more diffuse emission surrounding the region. They also observe that, on average, the X-rays spread poleward of the Ganymede footprint and extend to the Io footprint and beyond in regions near 225° SIII longitude. W21 also finds that the southern auroral emissions are far more diffuse over the ~20 year period and are mostly contained within the Ganymede footprint. From the average brightness map, there does not appear to be a concentrated region in the southern aurora as is observed in the north. Comparing these average heat maps to the polar plots displayed in Figure 6 will help to illustrate the dynamic variability of the X-ray aurora and identify any deviation from the nominal morphology.

Within the first full jovian rotation (JR1: 12:14 to 22:09 UT on 15 September 2021, top row of Figure 6) of our 40 hr Chandra HRC-I X-ray observation, 527 photons are detected in the north, with 199 detected in the south. The morphology of the northern auroral region in Figure 6a shows a concentrated region of X-ray emission (green) between ~60–70° SIII latitude and ~155–170° SIII longitude, which lies within the Ganymede footprint and coincides with the concentrated northern auroral region presented in W21. The surrounding diffuse emission (dark blue) extends beyond the Io footprint in the SIII longitude range ~150–230°. This polar heat map also includes the time interval for which we observed a statistically significant ~25 min QPP (19:10-20:38 UT on 15 September 2021) using the log(PSD) > 2.5 threshold. Conversely, the southern auroral emission in Figure 6b appears dim and diffuse with no bright concentrated region with almost all of the southern auroral emissions contained within the Ganymede footprint. During this time interval, the Juno MAG data show that the lobe magnetic field amplitude lies within the uncertainties of the Kivelson and Khurana (2002) lobe field fall-off model. This suggests that the magnetosphere is in a relaxed state, which would explain why the X-ray morphology mimics the average behavior from W21 for both the north and south poles.

In JR2 (15 September 22:09 to 16 September 08:05), a decrease in the brightness of the northern aurora (6c), with 397 photons (~25% drop from J1), is accompanied by an intense brightening (peak brightness 2.7 times brighter than JR1) of the southern emission poleward of the Ganymede footprint (6d), as 284 photons (increase of ~43%) are observed. This enhancement in the south is localized between ~−80 to −90° SIII latitude and spans a broad SIII longitude range between ~330-45°. The northern concentrated region shrinks in latitude, while the diffuse emission (in dark blue) also contracts to lie along the Io footprint. This deviation from the W21 average X-ray morphology coincides with the time interval containing the estimated arrival of a solar wind compression as predicted by the Tao et al. (2005) solar wind propagation model (see Figure 5), which impacted on Jupiter's magnetosphere at 02:00 UT on 16 September. The small JSE angle (<10°) during the time of the CXO window means that the uncertainties in the propagation time between Earth and Jupiter are minimized. Therefore, It should also be noted that while a brightening of the southern aurora is observed during this JR, no statistically significant QPPs are observed in the south over this time interval. There is an overlap of over 2 hr between the beginning of JR2 and the end of the first viewing of the northern envelope (NE1), finishing at 16 September 00:24, which is clearly visible in Figure 2. A statistically significant QPP with period of ~26 min is found during this 6 hr interval.

In JR3 (08:05 to 18:00 UT on 16 September 2021), we observe a broadening in SIII longitude of the northern auroral emission (467 counts, 6e), with the concentrated (green) emission shifting further toward 135° SIII longitude and toward the Ganymede footprint boundary. This is accompanied by a general enhancement equatorward
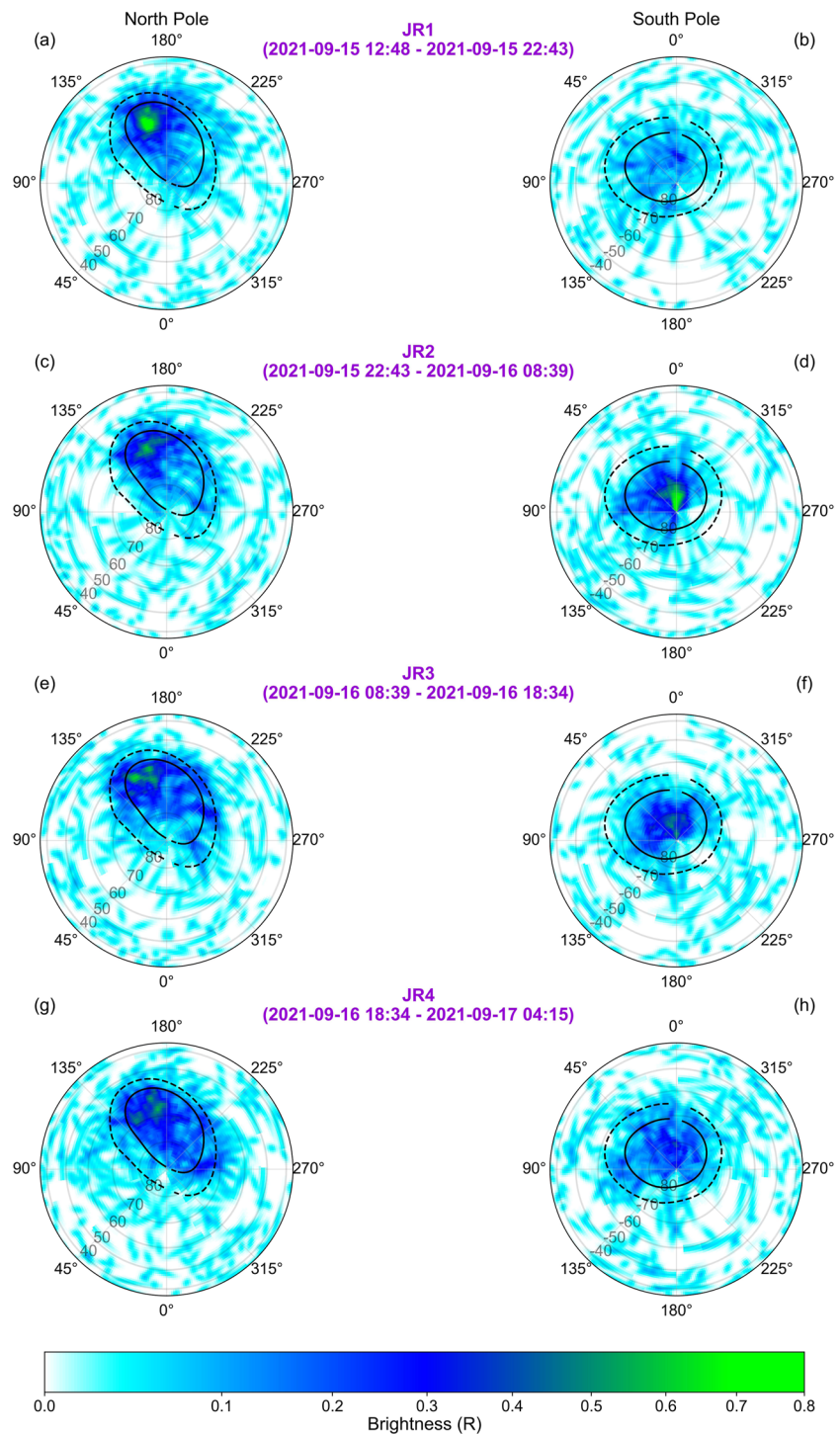
Figure 6. Polar X-ray heat maps of (left) Jupiter's north and (right) south poles as viewed from above. The plots have been split by jovian rotation (JR, ~10 hr), with start and end times shown in purple. The azimuth angle (in jovigraphic longitude) within the polar plot (in degrees) is indicated around the plot. The concentric circles represent 10° latitude increments. Overplotted are the footprints of Io (dashed black line) and Ganymede (solid black line), computed using the JRM33 model (Connerney et al., 2022) with the magnetodisk model of Connerney et al. (2020). The brightness of the X-ray emissions is proportional to the photon flux (calculated from the point spread function (PSF)) and is denoted by the color bar below in units of Rayleighs (R). The PSF shows the number density of photons detected with an uncertainty on its position. The regions that have little to no X-ray emissions are represented in white.

in the less concentrated (blue) emission from 135 to 270° SIII longitude toward the Io footprint. The southern emissions are comparable to the previous rotation (267 counts) in terms of count rate, but the concentrated emission region from JR2 has decreased in brightness by a factor of 1.8. The overall morphology remains similar, with the emission lying within the Ganymede footprint. During the second half of this time interval is when the Juno data predicts a compression event of Jupiter's magnetosphere in both the Waves and MAG data. The bKOM auroral radio emissions become activated on ∼15:00 UT on 16 September 2021, which coincides with an increase in the lobe magnetic field strength above the Kivelson and Khurana (2002) lobe field fall-off model. The onset of a compression event appears to have changed the morphology of the concentrated northern auroral emission region, which no longer resembles the "spot" or "tear-drop" feature that was displayed in W21.

JR4 (16 September 18:00 to 17 September 03:41) contains 544 counts for the northern region and 324 counts for the south. The morphology of the north (6g) shows many similarities with the previous JR (6e), whereby we again see emission extending beyond the Io footprint in the region ∼200–300° SIII longitude. One difference is that the concentrated emission appears to be located in two distinct features, which is not observed in the other heat maps. This morphology of the northern aurora is similar to the case study of Weigt et al. (2020), which was observed during compressed conditions of Jupiter's magnetosphere. The southern emission (6h) appears more diffusive and dimmer than the north, with its morphology becoming similar to that observed for the south in JR1 (6b), and also the average morphology for the southern X-rays from W21. Within this time window, we see a continued enhancement of the lobe magnetic field amplitude in data from the Juno MAG instrument, which peaks at 00:05 UT on 17 September 2021 (see bottom panel of Figure 4), that is indicative of a compression of the jovian magnetosphere. However, timing analysis of the X-ray photons within this interval did not identify any statistically significant QPPs in the north or south. The observed peak magnetic field amplitude signifies the beginning of the second magnetic unloading phase (decrease in lobe field strength) in our data set, which coincided with enhanced auroral images from HST observations in Yao et al. (2019). Enhancements in the bKOM emission also occur during periods of increasing lobe field strength (magnetic loading). Comparing to the X-ray results, we observe a slight enhancement in terms of photon counts in the X-ray emissions from JR3 to JR4, as the northern emissions increase by 16% and the southern emissions increase by 21%. However, this incremental increase in total counts does not translate to an increase in X-ray brightness, as the peak brightness decreases for both the northern and southern emissions.

4. Discussion and Conclusion

In this paper we present an extended observation of Jupiter's X-ray aurora, made over a 40-hr interval by the Chandra X-ray Observatory from 15 to 17 September 2021 during a solar wind compression event (as confirmed from both solar wind propagation model and in situ magnetic field data). The Chandra X-ray observation is complemented with in situ sampling of Jupiter's magnetic field and remote sensing of its radio emissions by the NASA Juno spacecraft. The addition of propagated solar wind model parameters also helps to shed light on the external drivers at work during this time interval.

Timing analysis reveals two intervals containing statistically significant quasi-periodic pulsations (QPPs) for the northern auroral X-rays: with periods of ∼25 and ∼26 min respectively, taking place during the first (JR1) and second (JR2) JRs of the 40-hr Chandra X-ray observation. The unique feature of this study is that, although Juno was far from the magnetopause and not directly measuring the solar wind, we have the ability to infer the state of magnetospheric compression using both Juno data and propagated solar wind data. The in situ and remote sensing spacecraft data reveal an intense activation of the broadband kilometric emission (bKOM) in the Juno Waves data, along with a sudden enhancement in the lobe magnetic field strength from Juno MAG. The (Tao et al., 2005) solar wind 1D MHD propagation model also predicts a strong enhancement in solar wind dynamic pressure which would have compressed the magnetosphere during the Chandra X-ray observation. Quasi-periods of ∼26 min were also found by Dunn et al. (2016), Weigt et al. (2020), and Wibisono et al. (2020) for Chandra and XMM-Newton X-ray observations of Jupiter that also coincided with inferred compression events. In these previous studies, it has been suggested that the quasi-periodic emissions may be a result of global ultra-low frequency (ULF) waves in the magnetic field, which are found to be a product of resonant responses of closed field lines to perturbations from magnetospheric mechanisms, including, but not limited to, Kelvin-Helmholtz instability (KHI) on the magnetopause boundary. Using Galileo data combined with modeling, Manners et al. (2018) found that ULF waves, associated with standing Alfvén wave activity, are observed throughout the jovian magnetosphere,

indicative of a global phenomenon. They are also observed to pulsate every ∼10–20 min, with occasional periods as long as 60 min (e.g., Khurana & Kivelson, 1989; Nichols, Yeoman, et al., 2017; Wilson & Dougherty, 2000). The range of periodicities may be a result of the changing thickness of the plasma sheet (Manners et al., 2018). During a compression event (such as that found during the Chandra observation interval), the plasma sheet is expected to thicken (Southwood & Kivelson, 2001), resulting in a longer period QPP. Conversely, during the relaxation phases of the magnetosphere, the plasma sheet thickness decreases along with the periodicity of the QPP (Manners et al., 2018).

ULF waves at Earth are often associated with dayside reconnection (Prikryl et al., 1998) or with either KHIs or compression events (Chandrasekhar, 1961; Dungey & Loughhead, 1954; Kivelson & Russell, 1995). For example, KHIs can trigger magnetopause fluctuations in Earth's magnetosphere and excite compressional ULF magnetic field oscillations and field line resonances, driving standing Alfvén waves in the ionosphere (Mann et al., 2002; Rae et al., 2005). KHIs can therefore be considered as means of propagating ULF wave activity from the outer jovian magnetosphere to the ionosphere (e.g., Manners & Masters, 2020). Kimura et al. (2016) found the X-ray count rates during a 2014 campaign to be positively correlated with solar wind velocity and insignificant with the dynamic pressure, and also stated the possibility that KHI events on the dusk flank at Jupiter could generate polar auroral variations. More work needs to be carried out to determine if KHIs can produce the field-aligned potential drops up to several MeV as required to produce the auroral X-rays (Cravens et al., 2003). However, wave-particle interactions, KHI-driven reconnection and/or modulation of current systems and their associated potential drops are all possible acceleration mechanisms (Dunn et al., 2017).

Alternatively, Yao et al. (2021) analyzed X-ray observations from 2017 coinciding with Juno's location in the predawn sector of the jovian magnetosphere, and showed that Jupiter's soft X-ray aurora pulsed in time with fluctuations in Jupiter's magnetic field strength occurring in the compressional direction of the field. The magnetospheric compressional mode wave power and X-ray emissions were found to pulse with a shared period of ∼25 min (Yao et al., 2021). The large-scale compressional waves trigger EMIC (electromagnetic ion cyclotron) waves, which operate on smaller scales, as resonances between the magnetic field and the ion gyration (Dunn, 2022; Yao et al., 2021). The EMIC waves then further drive atmospheric precipitation of energetic sulfur and oxygen ions along the magnetic fields via a pitch angle diffusion process, thus generating the X-ray auroral processes. Modeling results from Yao et al. (2021) show that EMIC waves observed by Juno would efficiently scatter oxygen and sulfur ions with energies ranging from 10 keV to 1 MeV, therefore confirming the capability of the pitch angle scattering process. Manners and Masters (2020) found that constant perturbations of the magnetopause, leading to injections of ULF waves into the magnetosphere, are consistent with the ULF activity on both the dayside and dusk-flank sectors of the outer magnetosphere. They find that the lowest ULF power is found in the most ULF-active regions, which could represent the large variability of the magnetic field topology in the resonance region over long timescales. This increase power/amplitude of ULF waves as they get closer into the planet may provide the energy needed to drive the electromagnetic ion cyclotron (EMIC) wave process suggested by Yao et al. (2021).

Compressional mode waves can be produced in the magnetosphere as a result of solar wind compressions (Cho et al., 2017). Another potential driver for producing compressional waves on the dayside magnetopause is magnetopause surface waves (Glassmeier, 1995; Plaschke et al., 2013). Compressional waves could also potentially be produced from high-speed plasma flows from the Vasyliunas cycle (Vasyliunas, 1983), which have been known to drive the transient aurora at Saturn (Yao et al., 2017). As has been mentioned previously, large potential drops would be required to accelerate heavy ions to produce X-ray aurora (Cravens et al., 2003). Yao et al. (2021) posits that it is possible for periodic precipitations of heavy ion to be accompanied by periodic or quasi-steady accelerations. Large potential drops near the poles in specific locations could provide the MeV accelerations of heavy ions needed for the observed auroral X-ray emissions. Such megavolt potential drops have been observed in Jupiter's polar region (Clark et al., 2017, 2020). The nondipolar nature of the magnetic field in Jupiter's north pole (Moore et al., 2018; Connerney et al., 2018) would then produce a multitude of mirror forces and potential drops and regions suitable for particles to drift into a loss cone (Yao et al., 2021).

Analysis of the spatial morphology of Jupiter's northern and southern X-ray auroral emissions show their dynamic variability over timescales of a JR. Different morphologies are observed for the north and south, and their emissions change independently of each other, as has been observed previously (Dunn et al., 2017; Jackman et al., 2018). This is most noticeable when moving from the first to the second JRs (JR1–JR2) in Figure 6, when

the northern auroral brightness decreases by ∼30%, but the brightness of the southern aurora increase by ∼270%. This is suggestive that different drivers are producing the northern and southern X-rays. The tilt angle of Jupiter's north pole toward Earth during the Chandra X-ray observation makes for more favorable viewing conditions in the north than the south, meaning that Chandra is more likely to observe QPPs in the north. The northern auroral region is brightest and most concentrated during the interval when statistically significant QPPs were present. These QPPs occur before the arrival of a shock front at Jupiter's magnetopause, as predicted by the Tao et al. (2005) solar wind propagation model. During this time, Juno Waves and MAG data also suggest that the magnetosphere is in a relaxed state at Juno's location in the lobe. On the arrival of the shock front, we see a change in the northern X-ray morphology away from the average behavior displayed in W21, and we observe a fragmented concentrated emission region that eventually splits into two distinct features in JR4. This morphology was also observed in Weigt et al. (2020), also taking place during a state of magnetospheric compression, whereby the X-ray emitting region did not resemble a concentrated "spot" of emission as is the nominal morphology. A possible explanation for this is that the concentrated auroral region may host two possible independent X-ray sources that are governed by separate drivers.

In the near future, full investigation of the remainder of Chandra's 2021 X-ray observing campaign of Jupiter is a key priority. The accumulation of exposure time enables future statistical studies of Jupiter's auroral X-rays, with the ability to compare with data from the Juno spacecraft. As Juno extends its coverage of the dusk sector of Jupiter's magnetosphere, it will further examine the region thought to be the most likely source region for driving of jovian X-rays. This rich data set of in situ particles and fields data will hopefully be supplemented by further remote X-ray observations of Jupiter by Chandra and XMM-Newton, and will help to pin down a driver of the auroral X-ray emissions. Additionally, the development of more sophisticated solar wind propagation models will play a key role, particularly as they try to reduce the uncertainties in propagation time to Jupiter.

Data Availability Statement

Data from the *NASA Chandra X-ray Observatory* observation used in this study are available on the *Chandra Data Archive* and *Chandra Source Catalogue* (https://cda.harvard.edu/chaser/). In this study, we use the Louis, Zarka, and Cecconi (2021) Juno Waves processed data set for estimated flux density (doi: 10.25935/6jg4-mk86). Calibrated Juno MAG data can be found on the *NASA Planetary Data System* using the doi: 10.17189/1519711 (Connerney, 2022). Tao et al. (2005) solar wind propagation model parameters are provided from the *Automated Multi-Dataset Analysis* (*AMDA*) database (Génot et al., 2021, http://amda.cdpp.eu/). The McEntee (2023) Zenodo repository (https://doi.org/10.5281/zenodo.8418559) contains all data analysis tools and code presented in this work.

References

Bhardwaj, A., Branduardi-Raymont, G., Elsner, R. F., Gladstone, G. R., Ramsay, G., Rodriguez, P., et al. (2005). Solar control on Jupiter's equatorial x-ray emissions: 26-29 November 2003 xmm-Newton observation. *Geophysical Research Letters*, *32*, 1–5. https://doi.org/10.1029/2004GL021497

Bhardwaj, A., Eisner, R. F., Gladstone, G. R., Waite, J. H., Branduardi-Raymont, G., Cravens, T. E., & Ford, P. G. (2006). Low-to middle-latitude x-ray emission from Jupiter. *Journal of Geophysical Research*, *111*(A11). https://doi.org/10.1029/2006JA011792

Bonfond, B., Vogt, M., Gérard, J.-C., Grodent, D., Radioti, A., & Coumans, V. (2011). Quasi-periodic polar flares at Jupiter: A signature of pulsed dayside reconnections? *Geophysical Research Letters*, *38*(2). https://doi.org/10.1029/2010gl045981

Branduardi-Raymont, G., Bhardwaj, A., Elsner, R. F., & Rodriguez, P. (2010). X-Rays from saturn: A study with xmm-Newton and chandra over the years 2002-05. *Astronomy and Astrophysics*, *510*, A73. https://doi.org/10.1051/0004-6361/200913110

Branduardi-Raymont, G., Bhardwaj, A., Elsner, R. F., Gladstone, G. R., Ramsay, G., Rodriguez, P., et al. (2007). Latest results on jovian disk x-rays from xmm-Newton. *Planetary and Space Science*, *55*, 1126–1134. https://doi.org/10.1016/j.pss.2006.11.017

Branduardi-Raymont, G., Elsner, R. F., Galand, M., Grodent, D., Cravens, T., Ford, P., et al. (2008). Spectral morphology of the x-ray emission from Jupiter's aurorae. *Journal of Geophysical Research*, *113*(A2). https://doi.org/10.1029/2007ja012600

Chandrasekhar, S. (1961). Hydrodynamic and hydromagnetic stability.

Cho, J.-H., Lee, D.-Y., Noh, S.-J., Kim, H., Choi, C. R., Lee, J., & Hwang, J. (2017). Spatial dependence of electromagnetic ion cyclotron waves triggered by solar wind dynamic pressure enhancements. *Journal of Geophysical Research: Space Physics*, *122*(5), 5502–5518. https://doi.org/10.1002/2016ja023827

Clark, G., Mauk, B. H., Haggerty, D., Paranicas, C., Kollmann, P., Rymer, A., et al. (2017). Energetic particle signatures of magnetic field-aligned potentials over Jupiter's polar regions. *Geophysical Research Letters*, *44*(17), 8703–8711. https://doi.org/10.1002/2017GL074366

Clark, G., Mauk, B. H., Kollmann, P., Paranicas, C., Bagenal, F., Allen, R. C., et al. (2020). Heavy ion charge states in Jupiter's polar magnetosphere inferred from auroral megavolt electric potentials. *Journal of Geophysical Research (Space Physics)*, *125*(9), e28052. https://doi.org/10.1029/2020JA028052

Connerney, J. E. P. (2022). Uno MAG CALIBRATED DATA J V1.0, JNO-J-3-FGM-CAL-V1.0 [dataset]. NASA Planetary Data System. https://doi.org/10.17189/1519711

Connerney, J. E. P., Benn, M., Bjarno, J., Denver, T., Espley, J., Jorgensen, J., et al. (2017). The juno magnetic field investigation. *Space Science Reviews*, *213*(1–4), 39–138. https://doi.org/10.1007/s11214-017-0334-z

Connerney, J. E. P., Kotsiaros, S., Oliversen, R. J., Espley, J. R., Joergensen, J. L., Joergensen, P. S., et al. (2018). A new model of Jupiter's magnetic field from juno's first nine orbits. *Geophysical Research Letters*, *45*(6), 2590–2596. https://doi.org/10.1002/2018GL077312

Connerney, J. E. P., Timmins, S., Herceg, M., & Joergensen, J. (2020). A jovian magnetodisc model for the juno era. *Journal of Geophysical Research: Space Physics*, *125*(10), e2020JA028138. https://doi.org/10.1029/2020ja028138

Connerney, J. E. P., Timmins, S., Oliversen, R., Espley, J., Joergensen, J., Kotsiaros, S., et al. (2022). A new model of Jupiter's magnetic field at the completion of juno's prime mission. *Journal of Geophysical Research: Planets*, *127*(2), e2021JE007055. https://doi.org/10.1029/2021je007055

Cravens, T. E., Clark, J., Bhardwaj, A., Elsner, R., Waite, J. H., Maurellis, A. N., et al. (2006). X-ray emission from the outer planets: Albedo for scattering and fluorescence of solar x rays. *Journal of Geophysical Research*, *7*(A7), 111. https://doi.org/10.1029/2005JA011413

Cravens, T. E., Howell, E., Waite, J. H., Jr., & Gladstone, G. R. (1995). Auroral oxygen precipitation at Jupiter. *Journal of Geophysical Research*, *100*(A9), 17153–17161. https://doi.org/10.1029/95ja00970

Cravens, T. E., Waite, J. H., Gombosi, T. I., Lugaz, N., Gladstone, G. R., Mauk, B. H., & MacDowall, R. J. (2003). Implications of Jovian X-ray emission for magnetosphere-ionosphere coupling. *Journal of Geophysical Research (Space Physics)*, *108*(A12), 1465. https://doi.org/10.1029/2003JA010050

Daubechies, I. (1990). The wavelet transform, time-frequency localization and signal analysis. *IEEE Transactions on Information Theory*, *36*(5), 961–1005. https://doi.org/10.1109/18.57199

Dungey, J. W., & Loughhead, R. E. (1954). Twisted magnetic fields in conducting Fluids. *Australian Journal of Physics*, *7*(1), 5. https://doi.org/10.1071/PH540005

Dunn, W. R. (2022). X-Ray emissions from the jovian system. In *Handbook of x-ray and gamma-ray astrophysics* (pp. 110–156). https://doi.org/10.1007/978-981-16-4544-0_73-1

Dunn, W. R., Branduardi-Raymont, G., Carter-Cortez, V., Campbell, A., Elsner, R., Ness, J.-U., et al. (2020). Jupiter's x-ray emission during the 2007 solar minimum. *Journal of Geophysical Research: Space Physics*, *125*(6), e2019JA027219. https://doi.org/10.1029/2019JA027219

Dunn, W. R., Branduardi-Raymont, G., Elsner, R. F., Vogt, M. F., Lamy, L., Ford, P. G., et al. (2016). The impact of an icme on the jovian x-ray aurora. *Journal of Geophysical Research: Space Physics*, *121*(3), 2274–2307. https://doi.org/10.1002/2015ja021888

Dunn, W. R., Branduardi-Raymont, G., Ray, L. C., Jackman, C. M., Kraft, R. P., Elsner, R. F., et al. (2017). The independent pulsations of Jupiter's northern and southern x-ray auroras. *Nature Astronomy*, *1*(11), 758–764. https://doi.org/10.1038/s41550-017-0262-6

Dunn, W. R., Gray, R., Wibisono, A. D., Lamy, L., Louis, C., Badman, S. V., et al. (2020). Comparisons between Jupiter's x-ray, uv and radio emissions and in-situ solar wind measurements during 2007. *Journal of Geophysical Research: Space Physics*, *125*(6), e2019JA027222. https://doi.org/10.1029/2019JA027222

Elsner, R. F., Lugaz, N., Waite, J. H., Cravens, T. E., Gladstone, G. R., Ford, P., et al. (2005a). Simultaneous chandra X ray, hubble space telescope ultraviolet, and ulysses radio observations of Jupiter's aurora. *Journal of Geophysical Research (Space Physics)*, *110*(A1), A01207. https://doi.org/10.1029/2004JA010717

Elsner, R. F., Ramsey, B. D., Waite, J. H., Rehak, P., Johnson, R. E., Cooper, J. F., & Swartz, D. A. (2005b). X-ray probes of magnetospheric interactions with Jupiter's auroral zones, the galilean satellites, and the io plasma torus. *Icarus*, *178*(2), 417–428. https://doi.org/10.1016/j.icarus.2005.06.006

Génot, V., Budnik, E., Jacquey, C., Bouchemit, M., Renard, B., Dufourg, N., et al. (2021). Automated multi-dataset analysis (amda): An on-line database and analysis tool for heliospheric and planetary plasma data. *Planetary and Space Science*, *201*, 105214. https://doi.org/10.1016/j.pss.2021.105214

Gladstone, G. R., Waite, J. H., Grodent, D., Lewis, W. S., Crary, F. J., Elsner, R. F., et al. (2002). A pulsating auroral X-ray hot spot on Jupiter. *Nature*, *415*(6875), 1000–1003. https://doi.org/10.1038/4151000a

Glassmeier, K. H. (1995). Ultralow-frequency pulsations: Earth and Jupiter compared. *Advances in Space Research*, *16*(4), 209–218. https://doi.org/10.1016/0273-1177(95)00232-4

Hill, T. W. (2001). The jovian auroral oval. *Journal of Geophysical Research*, *106*(A5), 8101–8107. https://doi.org/10.1029/2000JA000302

Houston, S., Cravens, T., Schultz, D., Gharibnejad, H., Dunn, W., Haggerty, D., et al. (2020). Jovian auroral ion precipitation: X-Ray production from oxygen and sulfur precipitation. *Journal of Geophysical Research: Space Physics*, *125*(2), e2019JA027007. https://doi.org/10.1029/2019ja027007

Jackman, C. M., Arridge, C. S., Slavin, J. A., Milan, S. E., Lamy, L., Dougherty, M. K., & Coates, A. J. (2010). In situ observations of the effect of a solar wind compression on saturn's magnetotail. *Journal of Geophysical Research*, *115*(A10). https://doi.org/10.1029/2010ja015312

Jackman, C. M., Knigge, C., Altamirano, D., Gladstone, R., Dunn, W., Elsner, R., et al. (2018). Assessing quasi-periodicities in jovian x-ray emissions: Techniques and heritage survey. *Journal of Geophysical Research: Space Physics*, *123*(11), 9204–9221. https://doi.org/10.1029/2018JA025490

Jansen, F., Lumb, D., Altieri, B., Clavel, J., Ehle, M., Erd, C., et al.s (2001). XMM-Newton observatory. I. The spacecraft and operations. *Astronomy and Astrophysics*, *365*(1), L1–L6. https://doi.org/10.1051/0004-6361:20000036

Kharchenko, V., Bhardwaj, A., Dalgarno, A., Schultz, D. R., & Stancil, P. C. (2008). Modeling spectra of the north and south Jovian x-ray auroras. *Journal of Geophysical Research*, *113*(A8). https://doi.org/10.1029/2008ja013062

Khurana, K. K., & Kivelson, M. G. (1989). On jovian plasma sheet structure. *Journal of Geophysical Research*, *94*(A9), 11791–11803. https://doi.org/10.1029/JA094iA09p11791

Kimura, T., Kraft, R., Elsner, R., Branduardi-Raymont, G., Gladstone, G., Tao, C., et al. (2016). Jupiter's x-ray and euv auroras monitored by chandra, xmm-Newton, and hisaki satellite. *Journal of Geophysical Research: Space Physics*, *121*(3), 2308–2320. https://doi.org/10.1002/2015ja021893

Kivelson, M. G., & Khurana, K. K. (2002). Properties of the magnetic field in the Jovian magnetotail. *Journal of Geophysical Research*, *107*(A8), SMP–23. https://doi.org/10.1029/2001ja000249

Kivelson, M. G., & Russell, C. T. (1995). Introduction to space physics.

Kurth, W., Gurnett, D. A., & Scarf, F. (1989). Jovian type iii radio bursts. *Journal of Geophysical Research*, *94*(A6), 6917–6924. https://doi.org/10.1029/ja094ia04p03505

Kurth, W., Hospodarsky, G., Kirchner, D., Mokrzycki, B., Averkamp, T., Robison, W., et al. (2017). The juno waves investigation. *Space Science Reviews*, *213*(1–4), 347–392. https://doi.org/10.1007/s11214-017-0396-y

Leahy, D., Elsner, R., & Weisskopf, M. (1983). On searches for periodic pulsed emission-the Rayleigh test compared to epoch folding. *The Astrophysical Journal*, *272*, 256–258. https://doi.org/10.1086/161288

Louarn, P., Roux, A., Perraut, S., Kurth, W., & Gurnett, D. (1998). A study of the large-scale dynamics of the Jovian magnetosphere using the Galileo Plasma Wave Experiment. *Geophysical Research Letters*, *25*(15), 2905–2908. https://doi.org/10.1029/98GL01774

Louis, C. K., Jackman, C. M., Hospodarsky, G., O'Kane Hackett, A., Devon-Hurley, E., Zarka, P., et al. (2023). Effect of a magnetospheric compression on Jovian radio emissions: In situ case study using juno data. *Journal of Geophysical Research: Space Physics*, *128*(9), e2022JA031155. https://doi.org/10.1029/2022JA031155

Louis, C. K., Zarka, P., & Cecconi, B. (2021). Juno/Waves estimated flux density Collection (Version 1.0) [dataset]. PADC/MASER. https://doi.org/10.25935/6jg4-mk86

Louis, C. K., Zarka, P., Dabidin, K., Lampson, P.-A., Magalhães, F. P., Boudouma, A., et al. (2021). Latitudinal beaming of Jupiter's radio emissions from juno/waves flux density measurements. *Journal of Geophysical Research: Space Physics*, *126*(10), e2021JA029435. https://doi.org/10.1029/2021JA029435

MacDowall, R., Kaiser, M., Desch, M., Farrell, W., Hess, R., & Stone, R. (1993). Quasiperiodic jovian radio bursts: Observations from the ulysses radio and plasma wave experiment. *Planetary and Space Science*, *41*(11–12), 1059–1072. https://doi.org/10.1016/0032-0633(93)90109-f

Mann, I. R., Voronkov, I., Dunlop, M., Donovan, E., Yeoman, T. K., Milling, D. K., et al. (2002). Coordinated ground-based and Cluster observations of large amplitude global magnetospheric oscillations during a fast solar wind speed interval. *Annales Geophysicae*, *20*(4), 405–426. https://doi.org/10.5194/angeo-20-405-2002

Manners, H., & Masters, A. (2020). The global distribution of ultralow-frequency waves in Jupiter's magnetosphere. *Journal of Geophysical Research (Space Physics)*, *125*(10), e28345. https://doi.org/10.1029/2020JA028345

Manners, H., Masters, A., & Yates, J. (2018). Standing alfvén waves in Jupiter's magnetosphere as a source of 10-to 60-min quasiperiodic pulsations. *Geophysical Research Letters*, *45*(17), 8746–8754. https://doi.org/10.1029/2018gl078891

Mardia, K. (1972). *Statistics of directional data: Probability and mathematical statistics*. Academic Press.

McEntee, S. (2023). Seanmcentee/cxo_juno_2021: Cxo_juno_2021 [software]. Zenodo. https://doi.org/10.5281/zenodo.8418559

McEntee, S. C., Jackman, C. M., Weigt, D. M., Dunn, W. R., Kashyap, V., Kraft, R., et al. (2022). Comparing Jupiter's equatorial x-ray emissions with solar x-ray flux over 19 years of the chandra mission. *Journal of Geophysical Research: Space Physics*, *127*(12), e2022JA030971. https://doi.org/10.1029/2022ja030971

Metzger, A. E., Luthey, J. L., Gilman, D. A., Hurley, K. C., Schnopper, H. W., Seward, F. D., & Sullivan, J. D. (1983). The detection of x rays from Jupiter. *Journal of Geophysical Research*, *88*(A10), 7731–7741. https://doi.org/10.1029/JA088iA10p07731

Moore, K. M., Yadav, R. K., Kulowski, L., Cao, H., Bloxham, J., Connerney, J. E. P., et al. (2018). A complex dynamo inferred from the hemispheric dichotomy of Jupiter's magnetic field. *Nature*, *561*(7721), 76–78. https://doi.org/10.1038/s41586-018-0468-5

Nichols, J., Badman, S. V., Bagenal, F., Bolton, S., Bonfond, B., Bunce, E., et al. (2017). Response of Jupiter's auroras to conditions in the interplanetary medium as measured by the hubble space telescope and juno. *Geophysical Research Letters*, *44*(15), 7643–7652. https://doi.org/10.1002/2017gl073029

Nichols, J. D., Yeoman, T. K., Bunce, E. J., Chowdhury, M. N., Cowley, S. W. H., & Robinson, T. R. (2017). Periodic emission within Jupiter's main auroral oval. *Geophysical Research Letters*, *44*(18), 9192–9198. https://doi.org/10.1002/2017GL074824

Ozak, N., Cravens, T. E., & Schultz, D. R. (2013). Auroral ion precipitation at Jupiter: Predictions for juno. *Geophysical Research Letters*, *40*(16), 4144–4148. https://doi.org/10.1002/grl.50812

Plaschke, F., Angelopoulos, V., & Glassmeier, K. H. (2013). Magnetopause surface waves: THEMIS observations compared to MHD theory. *Journal of Geophysical Research (Space Physics)*, *118*(4), 1483–1499. https://doi.org/10.1002/jgra.50147

Prikryl, P., Greenwald, R. A., Sofko, G. J., Villain, J. P., Ziesolleck, C. W. S., & Friis-Christensen, E. (1998). Solar-wind-driven pulsed magnetic reconnection at the dayside magnetopause, pc5 compressional oscillations, and field line resonances. *Journal of Geophysical Research*, *103*(A8), 17307–17322. https://doi.org/10.1029/97JA03595

Rae, I. J., Donovan, E. F., Mann, I. R., Fenrich, F. R., Watt, C. E. J., Milling, D. K., et al. (2005). Evolution and characteristics of global Pc5 ULF waves during a high solar wind speed interval. *Journal of Geophysical Research (Space Physics)*, *110*(A12), A12211. https://doi.org/10.1029/2005JA011007

Reiner, M. J., Fainberg, J., Stone, R. G., Kaiser, M. L., Desch, M. D., Manning, R., et al. (1993). Source characteristics of Jovian narrow-band kilometric radio emissions. *Journal of Geophysical Research*, *98*(E7), 13163–13176. https://doi.org/10.1029/93JE00536

Southwood, D. J., & Kivelson, M. G. (2001). A new perspective concerning the influence of the solar wind on the Jovian magnetosphere. *Journal of Geophysical Research*, *106*(A4), 6123–6130. https://doi.org/10.1029/2000JA000236

Tao, C., Kataoka, R., Fukunishi, H., Takahashi, Y., & Yokoyama, T. (2005). Magnetic field variations in the Jovian magnetotail induced by solar wind dynamic pressure enhancements. *Journal of Geophysical Research*, *110*(A11). https://doi.org/10.1029/2004ja010959

Treumann, R. A. (2006). The electron-cyclotron maser for astrophysical application. *Astronomy and Astrophysics Review*, *13*(4), 229–315. https://doi.org/10.1007/s00159-006-0001-y

Trümper, J. (1993). Rosat—A new look at the x-ray sky. *Science*, *260*(5115), 1769–1771. https://doi.org/10.1126/science.260.5115.1769

Vasyliunas, V. M. (1983). Physics of the Jovian magnetosphere. 11. Plasma distribution and flow. In *Physics of the Jovian magnetosphere* (pp. 395–453). https://doi.org/10.1017/CBO9780511564574.013

Vogt, M. F., Bunce, E. J., Kivelson, M. G., Khurana, K. K., Walker, R. J., Radioti, A., et al. (2015). Magnetosphere-ionosphere mapping at jupiter: Quantifying the effects of using different internal field models. *Journal of Geophysical Research: Space Physics*, *120*(4), 2584–2599. https://doi.org/10.1002/2014ja020729

Vogt, M. F., Kivelson, M. G., Khurana, K. K., Walker, R. J., Bonfond, B., Grodent, D., & Radioti, A. (2011). Improved mapping of Jupiter's auroral features to magnetospheric sources. *Journal of Geophysical Research*, *116*(A3). https://doi.org/10.1029/2010ja016148

Watanabe, H., Kita, H., Tao, C., Kagitani, M., Sakanoi, T., & Kasaba, Y. (2018). Pulsation characteristics of jovian infrared northern aurora observed by the Subaru ircs with adaptive optics. *Geophysical Research Letters*, *45*(21), 11–547. https://doi.org/10.1029/2018gl079411

Weigt, D. M., Gladstone, G. R., McEntee, S. C., Dunn, W. R., Kashyap, V. L., Jackman, C. M., et al. (2022). Chandra_x_ray_data_processing_pipeline [software]. Zenodo. https://doi.org/10.5281/zenodo.7380282

Weigt, D. M., Jackman, C. M., Dunn, W. R., Gladstone, G. R., Vogt, M. F., Wibisono, A. D., et al. (2020). Chandra observations of Jupiter's x-ray auroral emission during juno apojove 2017. *Journal of Geophysical Research: Planets*, *4*, 125. https://doi.org/10.1029/2019JE006262

Weigt, D. M., Jackman, C. M., Vogt, M. F., Manners, H., Dunn, W. R., Gladstone, G. R., et al. (2021). Characteristics of Jupiter's x-ray auroral hot spot emissions using chandra. *Journal of Geophysical Research: Space Physics*, *9*, 126. https://doi.org/10.1029/2021JA029243

Weisskopf, M. C., Tananbaum, H. D., Van Speybroeck, L. P., & O'Dell, S. L. (2000). Chandra X-ray observatory (CXO): Overview. In J. E. Truemper & B. Aschenbach (Eds.), *X-ray optics, instruments, and missions iii* (Vol. 4012, pp. 2–16). https://doi.org/10.1117/12.391545

Wibisono, A. D., Branduardi-Raymont, G., Coates, A. J., Dunn, W. R., & French, R. J. (2023). Jupiter's equatorial X-ray emissions over two solar cycles. *Monthly Notices of the Royal Astronomical Society*, *521*(4), 5596–5603. https://doi.org/10.1093/mnras/stad905

Wibisono, A. D., Branduardi-Raymont, G., Dunn, W. R., Coates, A. J., Weigt, D. M., Jackman, C. M., et al. (2020). Temporal and spectral studies by XMM-Newton of Jupiter's x-ray auroras during a compression event. *Journal of Geophysical Research: Space Physics*, *125*(5), e2019JA027676. https://doi.org/10.1029/2019JA027676

Wibisono, A. D., Branduardi-Raymont, G., Dunn, W. R., Kimura, T., Coates, A. J., Grodent, D., et al. (2021). Jupiter's X-ray aurora during UV dawn storms and injections as observed by XMM-Newton, Hubble, and Hisaki. *Monthly Notices of the Royal Astronomical Society*, *507*(1), 1216–1228. https://doi.org/10.1093/mnras/stab2218

Wilson, R. J., & Dougherty, M. K. (2000). Evidence provided by galileo of ultra low frequency waves within Jupiter's middle magnetosphere. *Geophysical Research Letters*, *27*(6), 835–838. https://doi.org/10.1029/1999GL010750

Yao, Z., Dunn, W. R., Woodfield, E. E., Clark, G., Mauk, B. H., Ebert, R. W., et al. (2021). Revealing the source of Jupiter's x-ray auroral flares. *Science Advances*, *7*(28), eabf0851. https://doi.org/10.1126/sciadv.abf0851

Yao, Z. H., Grodent, D., Kurth, W. S., Clark, G., Mauk, B. H., Kimura, T., et al. (2019). On the relation between jovian aurorae and the loading/unloading of the magnetic flux: Simultaneous measurements from juno, hubble space telescope, and hisaki. *Geophysical Research Letters*, *46*(21), 11632–11641. https://doi.org/10.1029/2019GL084201

Yao, Z. H., Radioti, A., Rae, I. J., Liu, J., Grodent, D., Ray, L. C., et al. (2017). Mechanisms of Saturn's near-noon transient aurora: In situ evidence from Cassini measurements. *Geophysical Research Letters*, *44*(22), 11217–11228. https://doi.org/10.1002/2017GL075108

Zarka, P. (1998). Auroral radio emissions at the outer planets: Observations and theories. *Journal of Geophysical Research*, *103*(E9), 20159–20194. https://doi.org/10.1029/98JE01323

Zarka, P., Cecconi, B., & Kurth, W. S. (2004). Jupiter's low-frequency radio spectrum from cassini/radio and plasma wave science (rpws) absolute flux density measurements. *Journal of Geophysical Research*, *109*(A9). https://doi.org/10.1029/2003JA010260

Zarka, P., Magalhães, F. P., Marques, M. S., Louis, C. K., Echer, E., Lamy, L., et al. (2021). Jupiter's auroral radio emissions observed by cassini: Rotational versus solar wind control, and components identification. *Journal of Geophysical Research: Space Physics*, *126*(10), e2021JA029780. https://doi.org/10.1029/2021JA029780

Zhang, B., Delamere, P., Ma, X., Burkholder, B., Wiltberger, M., Lyon, J., et al. (2018). Asymmetric kelvin-helmholtz instability at Jupiter's magnetopause boundary: Implications for corotation-dominated systems. *Geophysical Research Letters*, *45*(1), 56–63. https://doi.org/10.1002/2017gl076315